Nano Research 2018, 11(5): 2648–2657
https://doi.org/10.1007/s12274-017-1894-7
Research Article
ISSN 1998-0124
CN 11-5974/O4

An additive dripping technique using diphenyl ether for tuning perovskite crystallization for high-efficiency solar cells

Di Huang[1,2,3], Tenghooi Goh[2], Yifan Zheng[2], Zilun Qin[1,3], Jiao Zhao[1,3], Suling Zhao[1,3], Zheng Xu[1,3] (✉), and André D. Taylor[2] (✉)

[1] *Key Laboratory of Luminescence and Optical Information (Beijing Jiaotong University), Ministry of Education, Beijing 100044, China*
[2] *Department of Chemical and Environmental Engineering, Yale University, New Haven CT 06511, USA*
[3] *Institute of Optoelectronics Technology, Beijing Jiaotong University, Beijing 100044, China*

Received: 5 July 2017
Revised: 9 October 2017
Accepted: 20 October 2017

KEYWORDS
perovskite solar cells,
additive dripping,
crystallinity,
diphenyl ether (DPE)

ABSTRACT

Controlling the morphology of the $MAPbI_{3-x}Cl_x$ active layer has remained a challenge towards advancing perovskite solar cells (PvSCs). Here, we demonstrate that a low temperature additive dripping (AD) treatment step, using diphenyl ether (DPE), can significantly improve the power conversion efficiency (PCE), compared to the control device using chlorobenzene (CB), by 15% up to 16.64%, with a high current density (J_{SC}) of 22.67 mA/cm^2. We chose DPE for its small and appropriate dipole moment to adjust the solubility of the $MAPbI_{3-x}Cl_x$ precursor during the formation of the intermediate phase and the $MAPbI_{3-x}Cl_x$ phase. The low DPE vapor pressure provides a longer processing window for the removal of residual dimethylformamide (DMF), during the annealing process, for improved perovskite formation. Imaging and X-ray analysis both reveal that the $MAPbI_{3-x}Cl_x$ film exhibits enlarged grains with increased crystallinity. Together, these improvements result in reduced carrier recombination and hole trap-state density in the $MAPbI_{3-x}Cl_x$ film, while minimizing the hysteresis problem typical of PvSCs. These results show that the AD approach is a promising technique for improving PvSCs.

1 Introduction

Organometal halide perovskite solar cells (PvSCs) have been regarded as next-generation solar cells because of their low cost of materials and processing, facile production of flexible devices, and high device performance [1–4]. Most reports about highly efficient PvSCs involve incorporating perovskite materials into a mesoporous scaffold coupled with a high-temperature sintering procedure (typically 450 ˚C) [2, 5–7]. Concurrently, low temperature solution-processable planar heterojunction (PHJ) PvSCs have also drawn significant attention because of their convenient and inexpensive device processing [8, 9]. These p-i-n type PvSCs have often been made using PHJ sandwich structures of perovskite material formed in between a hole-transporting material and an electron-transporting material [10].

Address correspondence to Zheng Xu, zhengxu@bjtu.edu.cn; André D. Taylor, andre.taylor@yale.edu

Because the crystallinity, morphology, thickness, and surface coverage all play a crucial role in PHJ PvSCs device performance, research efforts have focused on tuning these parameters to yield a high quality perovskite layer. For example, two notable strategies include: (1) A "two-step casting" approach that involves successive spin coating or vacuum co-deposition of a metal halide and an alkylammonium halide. This method hinges on the interdiffusion of precursors to induce large grain features [11, 12], and (2) a "one-step coating" technique with a pre-mixed perovskite solution, accompanied by additional control steps including solvent engineering [13], thermal annealing [14], or processing solvent additives [15–17]. Among the one-step coating approaches, processing solvent additives have shown the most attractive results. For instance, Jen et al. mixed a small amount of 1,8-diiodooctane (DIO) into the perovskite precursor solutions to improve the crystallization of perovskite films [15]. Recently, Kim et al. [18] demonstrated that dripping chlorobenzene (CB) together with a small amount of DIO during spin coating of perovskite, also referred to as additive dripping (AD), resulted in an exceptionally smooth and uniformly covered perovskite surface. Although this AD treatment can help improve the device efficiency, there are some major drawbacks in using DIO. Due to the molecule's very high boiling point (332.5 °C at 760 mmHg), DIO is difficult to remove from the photoactive films during the drying stage following spin coating. Accordingly, numerous reports have revealed that DIO residue in the active layer can jeopardize device reproducibility and long-term stability [19–22]. In addition, since DIO can improve the solubility of $PbCl_2$ [15], the effect of the AD treatment with DIO for decreasing the solubility of perovskite precursor solutions is limited. To overcome these problems, we have identified an alternative additive, diphenyl ether (DPE) with a comparatively low boiling point of 258 °C, and a reasonable dipole moment of 1.17 D to enhance the AD treatment [23]. We note that our group and others have previously reported DPE to enhance polymer solar cell performance with thick active layers [24, 25]. For example, Nguyen et al. applied DPE in the PPDT2FBT:$PC_{70}BM$ device to improve efficiencies up to 9.39% in a ~ 300 nm thick active layer [26]. Heeger et al. reported small-bandgap polymer solar cells with maximized light absorption by the thick active layer and minimized recombination by the optimized lateral and vertical morphology via DPE processing to exhibit a high power conversion efficiency (PCE) of 9.40% [27]. However, the application and impact of DPE in PvSCs has not been thoroughly reported.

Herein, we demonstrate that AD treatment with DPE promotes a perovskite film with higher crystallinity and enlarged grain size. This results from the low dipole moment of DPE, suitable for tuning the solubility of $MAPbI_{3-x}Cl_x$ precursor, and the relatively lower vapor pressure, compared to that of CB, which provides a longer timeframe to remove residual dimethylformamide (DMF) for perovskite growth during the annealing process. Furthermore, the DPE-treated $MAPbI_{3-x}Cl_x$ film shows improved optical and morphological properties, which notably enhances the photocurrent density and efficiency (up to 22.67 mA/cm^2 and 16.7%, respectively) of PHJ PvSCs. More specifically, devices processed with DPE exhibit reduced carrier recombination and hole trap-state density. Based on these benefits, we suggest that our proposed AD treatment with DPE can be a simple yet valuable new strategy towards controlling the crystallization and morphology of PHJ PvSCs.

2 Experimental

Indium tin oxide (ITO) substrates with a sheet resistance of 15 Ω/square were cleaned with detergent and ultrasonicated in acetone followed by deionized water, and finally ethanol. The cleaned ITO substrates were dried by nitrogen gas and rested for 15 min in a petri dish before ultraviolet–ozone (UV–ozone) treatment to increase the work function of ITO. The aqueous based PEDOT:PSS was directly obtained from Clevios Al 4083 and filtered through polytetrafluoroethylene (PTFE) filters (0.45 μm) prior to thin film fabrication. The poly(3,4-ethylenedioxythiophene):polystyrene sulfonate (PEDOT:PSS) films were spin-casted using a spinning speed of 4,000 rpm/s and thermally annealed at 150 °C for 15 min in ambient atmosphere. The substrates were then transferred into a N_2-filled glove box for spin casting of the perovskite precursor solution. The perovskite precursor solution was prepared

using PbI_2 and CH_3NH_3I (molar ratio, 1:1 in DMF with 10 wt.% $PbCl_2$), and stirred overnight at 65 ˚C. The perovskite precursor concentration used was 1.8 mol/mL. Two perovskite films were deposited onto the ITO/PEDOT:PSS substrates (Fig. 1): (1) pristine $MAPbI_{3-x}Cl_x$ (CB): one step of spin coating at 7,500 rpm for 25 s using the perovskite precursor solution in 3.5 s followed by rapid dripping of 400 μL of CB onto the rotating substrate. (2) $MAPbI_{3-x}Cl_x$ (CB+DPE): one step of spin coating at 7,500 rpm for 25 s using the perovskite precursor solution in 3.5 s followed by rapid dripping of 400 μL of CB with DPE additive (1 vol.%) onto the rotating substrate. After drying the substrate at 100 ˚C for 5 min, phenyl-C61-butyric acid methyl ester ($PC_{61}BM$) solution (30 mg/mL in CB) was deposited onto the perovskite film. Finally, 5 nm of 4,7-diphenyl-1, 10-phenanthroline (Bphen, Luminescence Technology Corp.) and 100 nm of Ag were thermally evaporated at ~ 10^{-7} torr to form the contact electrodes. The architecture of the device is ITO/PEDOT:PSS/Perovskite/[6,6]-phenyl-C61-butyric acid methyl ester (PCBM)/Bphen/Ag (Fig. 1).

After fabrication, the devices were illuminated under a standard 100 mW/cm^2 simulated light source with AM 1.5 G filters (ABET Technologies). The illumination intensity was calibrated using a Newport calibrated Si solar cell with a quartz window. The active area of the device irradiated by the light was defined as 1.8 mm^2 using a photomask. This ensured that no excess current was collected outside of the defined area. Current density–voltage (*J*–*V*) data were acquired via a Keithley 2400 sourcemeter. The absorption and transmission spectra of dried films were obtained using a Shimadzu UV-3101 PC spectrometer. External quantum efficiency (EQE) measurements were performed in a nitrogen-filled glove box with a silicon cell calibrated QEPVSI system (Newport) under zero bias. Grazing incidence wide angle X-ray scattering (GIWAXS) data was obtained at beamline 1W1A, Beijing Synchrotron Radiation Facility (BSRF), using a Si (111) double crystal monochromator and a photon energy of 8 keV, with an incident angle of 0.2°. The scattering vector is given by $Q = 4\pi \sin\theta/\lambda$; θ is half of the total scattering angle, and λ is the X-ray wavelength (0.15476 nm). Scanning electron microscopy (SEM) images were obtained using a field emission Hitachi SU-70 unit. The absorption spectra of the films were acquired using a Varian Cary 3E UV-vis spectrophotometer. Time-resolved photoluminescence spectra (TR-PL) were measured using a time-correlated single photon counting measurement system with 470 nm excitation wavelength and 770 nm probing wavelength.

3 Results and discussion

In general, spin coating of a $MAPbI_{3-x}Cl_x$ precursor dissolved in DMF on a substrate is followed immediately by exposure of the wet film to the second solvent (CB) [13]. CB does not dissolve the perovskite materials and is miscible with DMF for freezing all constituents into a uniform layer. Upon removal of the residual DMF, a new intermediate complex phase is formed [28]. This complex is then converted into a highly uniform and crystalline perovskite film on annealing. Chemically, DPE is a major side product in the high-pressure hydrolysis of CB [29]. We compare the chemical structures for CB and DPE (Fig. S1(a) in the Electronic Supplementary Material (ESM)), and

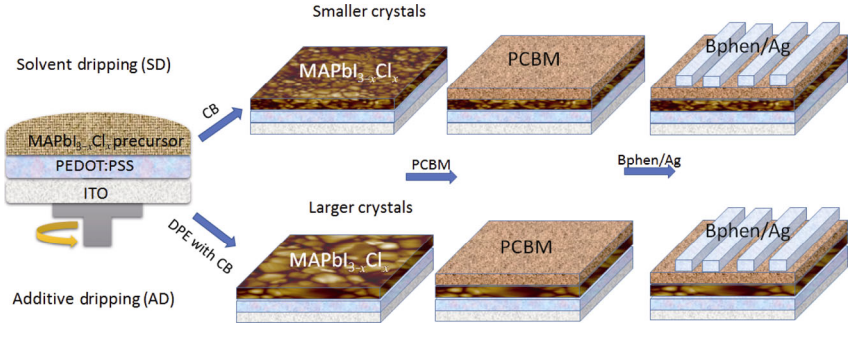

Figure 1 Schematic description for the fabrication of the device with $MAPbI_{3-x}Cl_x$ (CB) and $MAPbI_{3-x}Cl_x$ (DPE+CB) by time interval solvent-dripping without and with DPE, respectively, and the device architecture of the PvSCs constructed by ITO/PEDOT:PSS/Perovskite/PCBM/Bhpen/Ag.

demonstrate a limited solubility to the $MAPbI_{3-x}Cl_x$ precursor at room temperature with additions of CB and DPE (Fig. S1(b) in the ESM). DPE is a non-polar solvent with a dipole moment of 1.17 D versus for CB (1.54 D), which can induce transformation to the complex phase. Furthermore, DPE possesses a higher boiling point (258 ℃) than DMF (153 ℃) or CB (132 ℃), which means that it has a lower vapor pressure under standard processing conditions. Consequently, DPE needs more time than CB to be removed from the film. This provides a longer period of time for removing the residual DMF during the annealing process, and results in perovskite growth with high crystallinity. Moreover, it is possible to tune the kinetics of crystal growth of $MAPbI_{3-x}Cl_x$ by the DPE molecules remaining in the film [16, 30, 31]. These results indicate that $MAPbI_{3-x}Cl_x$ treated with DPE easily promotes better nucleation and growth in the perovskite film.

To investigate the impact of DPE on both lattice structure and crystallographic orientations of the perovskite, we employed synchrotron-based GIWAXS to probe the internal nanostructure of the pristine $MAPbI_{3-x}Cl_x$ (CB) and $MAPbI_{3-x}Cl_x$ (CB+DPE) films grown on ITO/PEDOT:PSS. The presence of strong scattering rings in both films indicates that the perovskite layers are predominantly polycrystalline (Fig. 2 and Fig. S2 in the ESM). The $MAPbI_{3-x}Cl_x$ films exhibit the anisotropic signals at q = 1, 2, 2.3, and 2.8 Å^{-1} which correspond to the (110), (220), (310), and (224) lattice planes, respectively. This indicates that all of the $MAPbI_{3-x}Cl_x$ films possess orthorhombic crystal structure [2, 32]. We note that the absence of the PbI_2 (001) scattering peak at q = 0.9 Å^{-1} indicates a complete conversion of the insulating PbI_2 into a semiconducting perovskite [33]. However, clearly sharper peaks (at 1.0, 2.0, 2.3, and 2.8 Å^{-1}) are seen for $MAPbI_{3-x}Cl_x$ (CB+DPE). The stronger perovskite scattering signals of (110), (220), (310), and (224) correspond to diffraction intensities of $MAPbI_{3-x}Cl_x$ (CB+DPE), and imply that the $MAPbI_{3-x}Cl_x$ (CB+DPE) granules are highly crystalline. Moreover, the full width at half maximum (FWHM), based on the Debye-Scherrer equation, is narrower for the $MAPbI_{3-x}Cl_x$ (CB+DPE) film (Table 1), which indicates better film crystallinity, crystal orientation, and larger grain sizes than pristine $MAPbI_{3-x}Cl_x$ (CB). We also note that the absorbance of the $MAPbI_{3-x}Cl_x$ (CB+DPE) film is higher than that of $MAPbI_{3-x}Cl_x$ (CB) in the range of 550–800 nm, which may come from better crystallization of $MAPbI_{3-x}Cl_x$ (CB+DPE), which is consistent with the results of Ren et al. [34]. These results demonstrate that the AD process benefits crystal formation, which in turn improves the optoelectronic device performance.

In order to study the impact of DPE on the morphology of the perovskite films, we obtained the top-view SEM images of the film surface after completion of annealing. The $MAPbI_{3-x}Cl_x$ (CB+DPE) film is pinhole-free and has full coverage on the substrate (Figs. 3(a) and 3(b)). The average grain size for the perovskite thin films with and without DPE treatment are 300 and 160 nm, respectively. The grain size distribution was extracted from the SEM images using the Nano Measurer 1.2 software (see Fig. S3 in the ESM) [35]. This observation is in accordance with

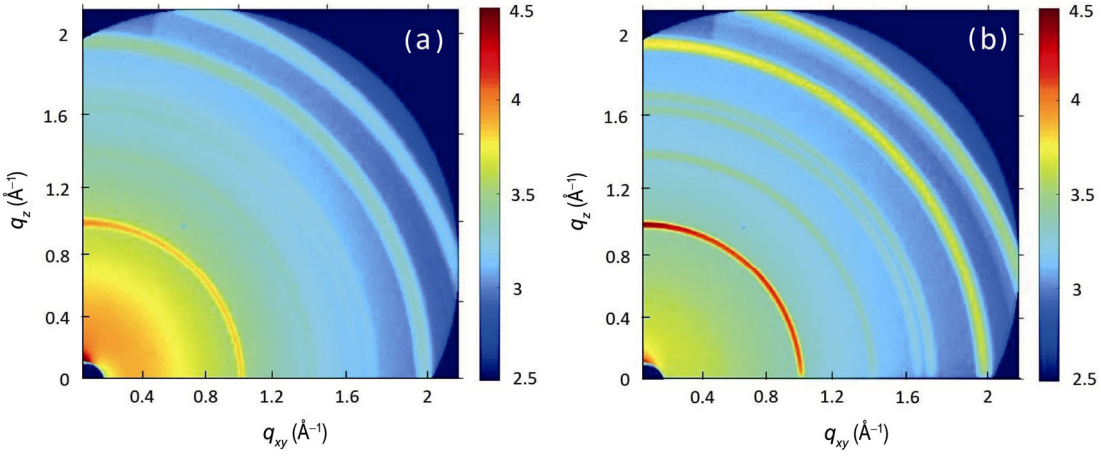

Figure 2 GIWAXS patterns for (a) pristine $MAPbI_{3-x}Cl_x$ (CB), and (b) $MAPbI_{3-x}Cl_x$ (CB+DPE) films formed on PEDOT:PSS.

Table 1 Values of FWHM at the peak of (110), and (220)

	FWHM ($Å^{-1}$)	
	(110)	(220)
$MAPbI_{3-x}Cl_x$ (CB)	0.105	0.115
$MAPbI_{3-x}Cl_x$ (CB+DPE)	0.048	0.082

the GIWAXS results, again revealing that the AD method favors the growth of large grain perovskite films. Together, these observations support the further study of using AD with solvents such as DPE towards preparing higher quality perovskite films for solar applications. The enlargement of the perovskite grain size is indicative of fewer grain boundaries and lower trap state density in the $MAPbI_{3-x}Cl_x$ (CB+DPE) film [36]. As the recombination of the PvSCs is governed by the trap states [37], the larger grain size of the $MAPbI_{3-x}Cl_x$ (CB+DPE) film suggests a lower probability of carrier recombination and loss.

Next, we investigated the variation in the optical properties of the pristine $MAPbI_{3-x}Cl_x$ (CB) and $MAPbI_{3-x}Cl_x$ (CB+DPE) films. The optical absorption spectra of the pristine $MAPbI_{3-x}Cl_x$ (CB) and $MAPbI_{3-x}Cl_x$ (CB+DPE) films on ITO/PEDOT:PSS are shown in Fig. 4(a). The thicknesses of the $MAPbI_{3-x}Cl_x$ (CB) and $MAPbI_{3-x}Cl_x$ (CB+DPE) films were about 490 and 496 nm, respectively. The absorbance of the $MAPbI_{3-x}Cl_x$ (CB+DPE) film is higher than that of the $MAPbI_{3-x}Cl_x$ (CB) in the range of 550–800 nm, which may be the result of better crystallization of $MAPbI_{3-x}Cl_x$ (CB+DPE), consistent with the results of Ren et al. [34]. This demonstrates that the $MAPbI_{3-x}Cl_x$ (CB+DPE) absorber can capture a greater photon flux to generate more carriers.

In order to probe the effect of the enhanced crystallization and morphology of the perovskite thin films that were prepared using the AD method, on charge dissociation, TR-PL spectra were obtained and analyzed. The corresponding PL spectra and decay curves for the pristine $MAPbI_{3-x}Cl_x$ (CB) and $MAPbI_{3-x}Cl_x$ (CB+DPE) films on the ITO/PEDOT:PSS substrate, with the incident laser beam coming from the substrate direction, are shown (Fig. 4(b) and Fig. S4 in the ESM). The excitation wavelength was set at 470 nm, which had a limited penetration depth in the perovskite films. This ensured that the study of the charge carrier behavior for the perovskite films was carried out close to the interface between the perovskite layer and the charge collection layers [38]. The TR-PL decays were acquired at an emission wavelength of 770 nm. Using the AD method, photo-generated carriers are extracted quickly to the PEDOT:PSS, causing a sharp decline of the PL peak for the $MAPbI_{3-x}Cl_x$ (CB+DPE) film. The PL decay curves were fitted with a bi-exponential decay function [39]. The ITO/PEDOT:PSS/$MAPbI_{3-x}Cl_x$ (CB) stack exhibits an average decay of 21 ns which is calculated by the following formula

$$< \tau > = \frac{\sum_{i}^{n} a_i \tau_i^2}{\sum_{i}^{n} a_i \tau_i} \quad (1)$$

where τ is the decay constant and n = 2. In the ITO/PEDOT:PSS/$MAPbI_{3-x}Cl_x$ (CB+DPE) stack, the average decay is reduced to 8 ns. This suggests that most of the free carriers generated on the $MAPbI_{3-x}Cl_x$ (CB+DPE) films are efficiently transferred to PEDOT:PSS minimizing carrier recombination, which confirms the potential of the conventional p-i-n heterojunction. This observation is also consistent with the reduced steady-state PL peak intensity and directly translates into an improved device performance.

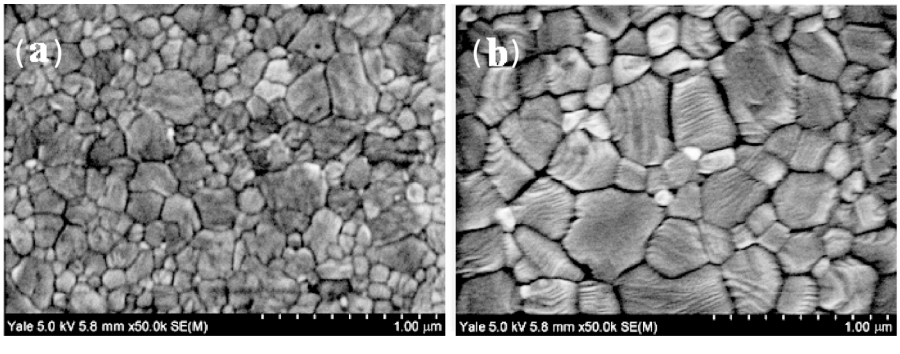

Figure 3 Top-view SEM images of (a) pristine $MAPbI_{3-x}Cl_x$ (CB) and (b) $MAPbI_{3-x}Cl_x$ (CB+DPE).

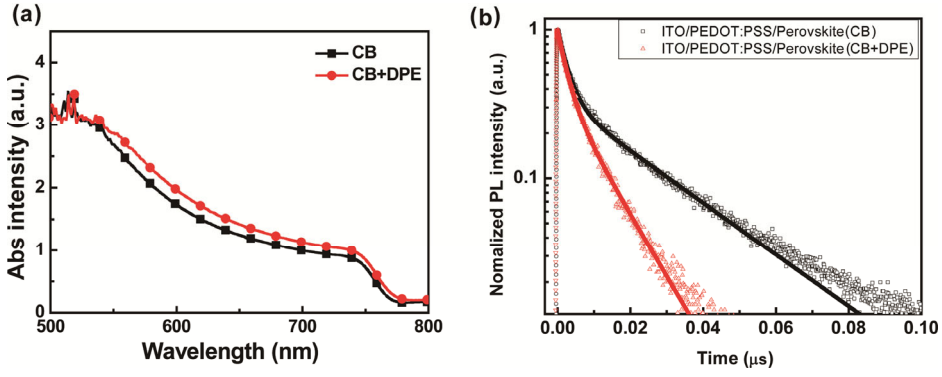

Figure 4 (a) Absorption spectra of (both) perovskite films; the data was normalized with respect to film thickness. (b) Time-resolved decay curves for both perovskite films.

Next, PvSCs were fabricated by using the pristine $MAPbI_{3-x}Cl_x$ (CB) and $MAPbI_{3-x}Cl_x$ (CB+DPE) films, and PCBM. The current density–voltage (*J*–*V*) curves under 100 mW/cm^2 are shown, where the performances of PvSCs composed of ITO/PEDOT:PSS/Perovskite/PCBM/Bphen/Ag fabricated using pristine $MAPbI_{3-x}Cl_x$ (CB) and $MAPbI_{3-x}Cl_x$ (CB+DPE) films are observed (Fig. 5(a)). The corresponding parameters are summarized in Table 2. As shown in Fig. 5(a) and Table 2, the PvSC device made with the $MAPbI_{3-x}Cl_x$ (CB) film exhibits a PCE (forward/reverse) of 13.94%/14.43% and a short-circuit current density (J_{sc}) (forward/reverse) of 19.12/19.87 mA/cm^2. They also show an open-circuit voltage (*V*oc) (forward/reverse) of 0.92/0.92 V, and fill factor (FF) (forward/reverse) of 79%/80%. On the other hand, the device made with the $MAPbI_{3-x}Cl_x$ (CB+DPE) film exhibits a PCE of 16.38%/16.64% with *J*sc = 22.67/22.74 mA/cm^2, *V*oc = 0.93/0.94 V, and FF = 78%/78%. Remarkably, we demonstrate that the forward and reverse current densities from the PvSCs incorporated with the $MAPbI_{3-x}Cl_x$ (CB+DPE) are significantly enhanced when compared with those from the PvSCs incorporated with the pristine $MAPbI_{3-x}Cl_x$ (CB). This is confirmed by the incident photocurrent efficiency (IPCE) in Fig. 5(b). The calculated *J*sc increased after using DPE+CB treated perovskite films, which is consistent with the *J*sc enhancement from the *J*–*V* curve. We surmise that the *J*sc improvement may originate from the enhanced absorption and superior crystallinity of the perovskite film prepared using DPE. As a result, about 15% enhancement in PCE is observed from the PvSCs incorporated with the $MAPbI_{3-x}Cl_x$ (CB+DPE). The statistical analyses of the maximum PCE collected from ten independent devices fabricated using different batches are shown (Fig. S5 and Table S1 in the ESM). This confirms the improvements observed in films made with DPE. We emphasize that the high PCEs (over 16%) observed from this study are achieved by low-temperature solution-processed PvSCs made of a rather simple device structure, opens a new trail towards efficient and low-cost photovoltaics.

The hysteresis problem in $MAPbI_{3-x}Cl_x$ systems has

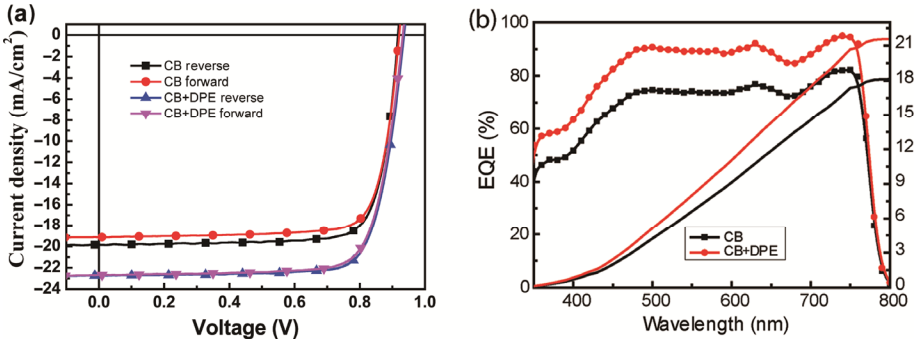

Figure 5 Photovoltaic metrics of perovskite solar cells with and without DPE. (a) *J*–*V* curves were measured at a scan rate of 142 mV/s under AM1.5 simulated solar light (100 mW/cm^2). (b) Incident photon-to-current efficiency (IPCE) curves and corresponding integrated *J*sc curves for the devices with pristine $MAPbI_{3-x}Cl_x$ (CB), and $MAPbI_{3-x}Cl_x$ (CB+DPE) perovskite films.

Table 2 Photovoltaic performances of the best PvSCs with pristine $MAPbI_{3-x}Cl_x$ (CB), and $MAPbI_{3-x}Cl_x$ (CB+DPE) perovskite films

	Scan direction	J_{sc} (mA/cm^2)	V_{OC} (V)	FF (%)	PCE (%)
$MAPbI_{3-x}Cl_x$ (CB)	Forward	19.12	0.92	80	13.94
	Reverse	19.87	0.92	79	14.43
$MAPbI_{3-x}Cl_x$ (CB+DPE)	Forward	22.67	0.93	78	16.38
	Reverse	22.74	0.94	78	16.64

raised many concerns about the feasibility and long-term stability of this kind of photovoltaic technology [40, 41]. For the system described in this work, we illustrate that the *J*–*V* curves almost overlap for the forward and reverse scan directions (Fig. 5(a) and Table 2), which means that the *J*–*V* hysteresis is significantly minimized by the presence of DPE. It has been suggested that the following factors can potentially contribute to *J*–*V* hysteresis: trap-sites in the perovskite, charge transfer imbalance at the interface, and the capacitive effect due to extremely large values of photoinduced dielectricity [42–45]. To better understand our system, we conducted dark current–voltage (*I*–*V*) analysis on a hole-only device to quantify the hole trap-state density in the perovskite films. We display the *I*–*V* curves of the hole-only device using pristine $MAPbI_{3-x}Cl_x$ (CB) and $MAPbI_{3-x}Cl_x$ (CB+DPE) films in the dark (Fig. 6). The linear relation (green line) indicates an ohmic response of the hole-only device at the low bias voltage. As the bias voltage exceeds the kink point, the current rises nonlinearly (red line), signifying that the trap states are entirely filled. The trap-filled limit voltage (V_{TFL}) was determined by the trap-state density relation [46]

$$V_{TFL} = \frac{en_t L}{2\varepsilon\varepsilon_o} \quad (2)$$

where e is the elementary charge of the electron, L is the thickness of the perovskite film, ε_o is the vacuum permittivity, ε is the relative dielectric constant of perovskite (ε = 28.8) [47], and n_t is the trap-state density. V_{TFL} can be obtained from the kink point in the dark *I*–*V* curve. The $MAPbI_{3-x}Cl_x$ (CB) film coated on the ITO/PEDOT:PSS substrates has a hole trap-state density of 1.37 × 10^{16} cm^{-3}. As expected, when the $MAPbI_{3-x}Cl_x$ (CB+DPE) film was coated on the ITO/PEDOT:PSS, the hole trap-state density fell to 9.07 × 10^{15} cm^{-3}. A decrease of the trap density by 34% explains why the *J*–*V* hysteresis is almost entirely subdued in the PvSCs with DPE and thus contributes to the observed *J*sc increase [48, 49].

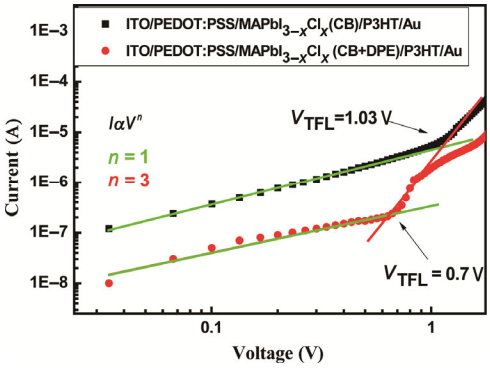

Figure 6 Dark *I*–*V* curves of the hole-only device revealing V_{TFL} kink point behavior.

4 Conclusions

In summary, by fine-tuning the solubility of $MAPbI_{3-x}Cl_x$ precursors and opening a longer time frame for $MAPbI_{3-x}Cl_x$ growth using an AD step with DPE, we achieve uniform, pinhole free perovskite films with improved crystallinity and larger grain size. This room-temperature solvent AD step is easy to implement using a small amount of DPE in CB that is briefly dripped during the spin casting step. Solar cells fabricated via AD of perovskite films with DPE exhibit PCEs up to 16.64%, with very small hysteresis due to three aspects: the absorption enhancement, the more efficient charge extraction, and the reduced recombination. AD also allows the development of $MAPbI_{3-x}Cl_x$ films with reduced carrier recombination. The results of this study introduce a new path for the development of high-efficiency PvSCs and we propose that further studies on employing the solvent AD approach for other solvents could potentially yield further improvements.

Acknowledgements

The authors gratefully acknowledge the Fundamental Research Funds for the Central Universities (No. S16JB00060), the National Science Foundation, NSF-PECASE award (No. CBET-0954985) and the National Natural Science Foundation of China (No. 61575019) for partial support of this work. D. H. also thanks the

support from the China Scholarship Council. The AFM SEM used were supported by the Yale Institute for Nanoscience and Quantum Engineering (YINQE) and NSF MRSEC DMR 1119826 for Center for Research on Interface Structures and Phenomena (CRISP). The GIWAXS obtained at 1W1A, BSRF. The authors further thank scientists of Diffuse X-ray Scattering Station in the experiments for the assistance with GIWAXS measurements, as well as Dr. Yuchuan Shao from the Department of Electrical Engineering, Yale University for the useful discussion.

Electronic Supplementary Material: Supplementary material (further details of GIXR measurements, the grain size statistical diagram, steady-state PL spectra and Box plot of the PCE) is available in the online version of this article at https://doi.org/10.1007/s12274-017-1894-7.

References

[1] Heo, J. H.; Im, S. H.; Noh, J. H.; Mandal, T. N.; Lim, C.-S.; Chang, J. A.; Lee, Y. H.; Kim, H.-J.; Sarkar, A.; Nazeeruddin, M. K. et al. Efficient inorganic-organic hybrid heterojunction solar cells containing perovskite compound and polymeric hole conductors. *Nat. Photonics* **2013**, *7*, 486–491.

[2] Lee, M. M.; Teuscher, J.; Miyasaka, T.; Murakami, T. N.; Snaith, H. J. Efficient hybrid solar cells based on meso-superstructured organometal halide perovskites. *Science* **2012**, *338*, 643–647.

[3] Kim, H.; Lim, K.-G.; Lee, T.-W. Planar heterojunction organometal halide perovskite solar cells: Roles of interfacial layers. *Energy Environ. Sci.* **2016**, *9*, 12–30.

[4] Meng, L.; You, J. B.; Guo, T.-F.; Yang, Y. Recent advances in the inverted planar structure of perovskite solar cells. *Acc. Chem. Res.* **2015**, *49*, 155–165.

[5] Saliba, M.; Matsui, T.; Seo, J.-Y.; Domanski, K.; Correa-Baena, J.-P.; Nazeeruddin, M. K.; Zakeeruddin, S. M.; Tress, W.; Abate, A.; Hagfeldt, A. et al. Cesium-containing triple cation perovskite solar cells: Improved stability, reproducibility and high efficiency. *Energy Environ. Sci.* **2016**, *9*, 1989–1997.

[6] Mei, A. Y.; Li, X.; Liu, L. F.; Ku, Z. L.; Liu, T. F.; Rong, Y. G.; Xu, M.; Hu, M.; Chen, J. Z.; Yang, Y. et al. A hole-conductor–free, fully printable mesoscopic perovskite solar cell with high stability. *Science* **2014**, *345*, 295–298.

[7] Ball, J. M.; Lee, M. M.; Hey, A.; Snaith, H. J. Low-temperature processed meso-superstructured to thin-film perovskite solar cells. *Energy Environ. Sci.* **2013** , *6*, 1739–1743.

[8] Jeng, J. Y.; Chiang, Y. F.; Lee, M. H.; Peng, S. R.; Guo, T. F.; Chen, P.; Wen, T. C. $CH_3NH_3PbI_3$ perovskite/fullerene planar-heterojunction hybrid solar cells. *Adv. Mater.* **2013**, *25*, 3727–3732.

[9] Gong, X.; Li, M.; Shi, X. B.; Ma, H.; Wang, Z. K.; Liao, L. S. Controllable perovskite crystallization by water additive for high-performance solar cells. *Adv. Funct. Mater.* **2015**, *25*, 6671–6678.

[10] Li, Y.; Xu, Z.; Zhao, S. L.; Qiao, B.; Huang, D.; Zhao, L.; Zhao, J.; Wang, P.; Zhu, Y. Q.; Li, X. G. et al. Highly efficient p-i-n perovskite solar cells utilizing novel low-temperature solution-processed hole transport materials with linear π-conjugated structure. *Small* **2016**, *12*, 4902–4908.

[11] Xiao, Z. G.; Bi, C.; Shao, Y. C.; Dong, Q. F.; Wang, Q.; Yuan, Y. B.; Wang, C. G.; Gao, Y. L.; Huang, J. S. Efficient, high yield perovskite photovoltaic devices grown by interdiffusion of solution-processed precursor stacking layers. *Energy Environ. Sci.* **2014**, *7*, 2619–2623.

[12] Hsiao, S. Y.; Lin, H. L.; Lee, W. H.; Tsai, W. L.; Chiang, K. M.; Liao, W. Y.; Ren-Wu, C. Z.; Chen, C. Y.; Lin, H. W. Efficient all-vacuum deposited perovskite solar cells by controlling reagent partial pressure in high vacuum. *Adv. Mater.* **2016**, *28*, 7013–7019.

[13] Xiao, M. D.; Huang, F. Z.; Huang, W. C.; Dkhissi, Y.; Zhu, Y.; Etheridge, J.; Gray-Weale, A.; Bach, U.; Cheng, Y. B.; Spiccia, L. A fast deposition-crystallization procedure for highly efficient lead iodide perovskite thin-film solar cells. *Angew. Chem.* **2014**, *126*, 10056–10061.

[14] Sun, S. Y.; Salim, T.; Mathews, N.; Duchamp, M.; Boothroyd, C.; Xing, G. C.; Sum, T. C.; Lam, Y. M. The origin of high efficiency in low-temperature solution-processable bilayer organometal halide hybrid solar cells. *Energy Environ. Sci.* **2014**, *7*, 399–407.

[15] Liang, P. W.; Liao, C. Y.; Chueh, C. C.; Zuo, F.; Williams, S. T.; Xin, X. K.; Lin, J.; Jen, A. K. Y. Additive enhanced crystallization of solution-processed perovskite for highly efficient planar-heterojunction solar cells. *Adv. Mater.* **2014**, *26*, 3748–3754.

[16] Song, X.; Wang, W. W.; Sun, P.; Ma, W. L.; Chen, Z.-K. Additive to regulate the perovskite crystal film growth in planar heterojunction solar cells. *Appl. Phys. Lett.* **2015**, *106*, 033901.

[17] Wei, Q. B.; Yang, D.; Yang, Z.; Ren, X. D.; Liu, Y. C.; Feng, J. S.; Zhu, X. J.; Liu, S. Z. Effective solvent-additive enhanced crystallization and coverage of absorber layers for high efficiency formamidinium perovskite solar cells. *RCS Adv.* **2016**, *6*, 56807–56811.

[18] Kim, H.; Jeong, H.; Lee, J. K. Highly efficient, reproducible, uniform $(CH_3NH_3)PbI_3$ layer by processing additive dripping for solution-processed planar heterojunction perovskite solar cells. *Chem.–Asian J.* **2016**, *11*, 2399–2405.

[19] Li, N.; Brabec, C. J. Air-processed polymer tandem solar cells with power conversion efficiency exceeding 10%. *Energy Environ. Sci.* **2015**, *8*, 2902–2909.

[20] Tremolet de Villers, B. J.; O'Hara, K. A.; Ostrowski, D. P.; Biddle, P. H.; Shaheen, S. E.; Chabinyc, M. L.; Olson, D. C.; Kopidakis, N. Removal of residual diiodooctane improves photostability of high-performance organic solar cell polymers. *Chem. Mater.* **2016**, *28*, 876–884.

[21] Ye, L.; Jing, Y.; Guo, X.; Sun, H.; Zhang, S. Q.; Zhang, M. J.; Huo, L. J.; Hou, J. H. Remove the residual additives toward enhanced efficiency with higher reproducibility in polymer solar cells. *J. Phys. Chem. C* **2013**, *117*, 14920–14928.

[22] Lee, S.; Kong, J.; Lee, K. Air-stable organic solar cells using an iodine-free solvent additive. *Adv. Energy Mater.* **2016**, *6*, 1600970.

[23] Chae, G. J.; Jeong, S.-H.; Baek, J. H.; Walker, B.; Song, C. K.; Seo, J. H. Improved performance in TIPS-pentacene field effect transistors using solvent additives. *J. Mater. Chem. C* **2013**, *1*, 4216–4221.

[24] Zheng, Y. F.; Goh, T.; Fan, P.; Shi, W.; Yu, J. S.; Taylor, D. A. Toward efficient thick active PTB7 photovoltaic layers using diphenyl ether as a solvent additive. *ACS Appl. Mater. Interfaces* **2016**, *8*, 15724–15731.

[25] Zhao, J.; Zhao, S. L.; Xu, Z.; Qiao, B.; Huang, D.; Zhao, L.; Li, Y.; Zhu, Y. Q.; Wang, P. Revealing the effect of additives with different solubility on the morphology and the donor crystalline structures of organic solar cells. *ACS Appl. Mater. Interfaces* **2016**, *8*, 18231–18237.

[26] Nguyen, T. L.; Choi, H.; Ko, S.-J.; Uddin, M. A.; Walker, B.; Yum, S.; Jeong, J.-E.; Yun, M. H.; Shin, T. J.; Hwang, S. et al. Semi-crystalline photovoltaic polymers with efficiency exceeding 9% in a ~300 nm thick conventional single-cell device. *Energy Environ. Sci.* **2014**, *7*, 3040–3051.

[27] Choi, H.; Ko, S. J.; Kim, T.; Morin, P. O.; Walker, B.; Lee, B. H.; Leclerc, M.; Kim, J. Y.; Heeger, A. J. Small-bandgap polymer solar cells with unprecedented short-circuit current density and high fill factor. *Adv. Mater.* **2015**, *27*, 3318–3324.

[28] Jeon, N. J.; Noh, J. H.; Kim, Y. C.; Yang, W. S.; Ryu, S.; Seok, S. I. Solvent engineering for high-performance inorganic–organic hybrid perovskite solar cells. *Nat. Mater.* **2014**, *13*, 897–903.

[29] Fahlbusch, K. G.; Hammerschmidt, F. J.; Panten, J.; Pickenhagen, W.; Schatkowski, D.; Bauer, K.; Garbe, D.; Surburg, H. Flavors and fragrances. In *Ullmann's Encyclopedia of Industrial Chemistry*. Wiley-VCH, Weinheim, 2002.

[30] Dualeh, A.; Tétreault, N.; Moehl, T.; Gao, P.; Nazeeruddin, M. K.; Grätzel, M. Effect of annealing temperature on film morphology of organic–inorganic hybrid pervoskite solid-state solar cells. *Adv. Funct. Mater.* **2014**, *24*, 3250–3258.

[31] Wu, Y. Z.; Islam, A.; Yang, X. D.; Qin, C. J.; Liu, J.; Zhang, K.; Peng, W. Q.; Han, L. Y. Retarding the crystallization of PbI_2 for highly reproducible planar-structured perovskite solar cells via sequential deposition. *Energy Environ. Sci.* **2014**, *7*, 2934–2938.

[32] Colella, S.; Mosconi, E.; Fedeli, P.; Listorti, A.; Gazza, F.; Orlandi, F.; Ferro, P.; Besagni, T.; Rizzo, A.; Calestani, G. et al. $MAPbI_{3-x}Cl_x$ mixed halide perovskite for hybrid solar cells: The role of chloride as dopant on the transport and structural properties. *Chem. Mater.* **2013**, *25*, 4613–4618.

[33] Tan, K. W.; Moore, D. T.; Saliba, M.; Sai, H.; Estroff, L. A.; Hanrath, T.; Snaith, H. J.; Wiesner, U. Thermally induced structural evolution and performance of mesoporous block copolymer-directed alumina perovskite solar cells. *ACS Nano* **2014**, *8*, 4730–4739.

[34] Ren, X. D.; Yang, Z.; Yang, D.; Zhang, X.; Cui, D.; Liu, Y. C.; Wei, Q. B.; Fan, H. B.; Liu, S. Z. Modulating crystal grain size and optoelectronic properties of perovskite films for solar cells by reaction temperature. *Nanoscale* **2016**, *8*, 3816–3822.

[35] Sun, W. H.; Li, Y. L.; Xiao, Y.; Zhao, Z. R.; Ye, S. Y.; Rao, H. X.; Ting, H.; Bian, Z. Q.; Xiao, L. X.; Huang, C. H. et al. An ammonia modified PEDOT:PSS for interfacial engineering in inverted planar perovskite solar cells. *Org. Electron.* **2017**, *46*, 22–27.

[36] Bi, C.; Wang, Q.; Shao, Y.; Yuan, Y. B.; Xiao, Z. G.; Huang, J. S. Non-wetting surface-driven high-aspect-ratio crystalline grain growth for efficient hybrid perovskite solar cells. *Nat. Commun.* **2015**, *6*, 7747.

[37] Wetzelaer, G.-J. A. H.; Max, S.; Araceli Miquel, S.; Cristina, M.; Jorge, Á.; Bolink, J. H. Trap-assisted non-radiative recombination in organic-inorganic perovskite solar cells. *Adv. Mater.* **2015**, *27*, 1837–1841.

[38] Shao, Y. C.; Xiao, Z. G.; Bi, C.; Yuan, Y. B.; Huang, J. S. Origin and elimination of photocurrent hysteresis by fullerene passivation in $CH_3NH_3PbI_3$ planar heterojunction solar cells. *Nat. Commun.* **2014**, *5*, 5784.

[39] Yamada, Y.; Nakamura, T.; Endo, M.; Wakamiya, A.; Kanemitsu, Y. Photocarrier recombination dynamics in perovskite $CH_3NH_3PbI_3$ for solar cell applications. *J. Am. Chem. Soc.* **2014**, *136*, 11610–11613.

[40] Ke, W. J.; Zhao, D. W.; Grice, C. R.; Cimaroli, A. J.; Ge, J.; Tao, H.; Lei, H. W.; Fang, G. J.; Yan, Y. F. Efficient planar perovskite solar cells using room-temperature vacuum-processed C_{60} electron selective layers. *J. Mater. Chem. A* **2015**, *3*, 17971–17976.

[41] Huang, D.; Goh, T.; Kong, J.; Zheng, Y. F.; Zhao, S. L.; Xu, Z.; Taylor, A. D. Perovskite solar cells with a DMSO-treated PEDOT:PSS hole transport layer exhibit higher photovoltaic performance and enhanced durability. *Nanoscale* **2017**, *9*, 4236–4243.

[42] Heo, J. H.; Song, D. H.; Han, H. J.; Kim, S. Y.; Kim, J. H.; Kim,

D.; Shin, H. W.; Ahn, T. K.; Wolf, C.; Lee, T. W. et al. Planar $CH_3NH_3PbI_3$ perovskite solar cells with constant 17.2% average power conversion efficiency irrespective of the scan rate. *Adv. Mater.* **2015**, *27*, 3424–3430.

[43] Wu, B.; Fu, K. W.; Yantara, N.; Xing, G. C.; Sun, S. Y.; Sum, T. C.; Mathews, N. Charge accumulation and hysteresis in perovskite-based solar cells: An electro-optical analysis. *Adv. Energy Mater.* 2015, *5*, 1500829.

[44] Unger, E. L.; Hoke, E. T.; Bailie, C. D.; Nguyen, W. H.; Bowring, A. R.; Heumüller, T.; Christoforo, M. G.; McGehee, M. D. Hysteresis and transient behavior in current–voltage measurements of hybrid-perovskite absorber solar cells. *Energy Environ. Sci.* **2014**, *7*, 3690–3698.

[45] Sanchez, R. S.; Gonzalez-Pedro, V.; Lee, J.-W.; Park, N.-G.; Kang, Y. S.; Mora-Sero, I.; Bisquert, J. Slow dynamic processes in lead halide perovskite solar cells. Characteristic times and hysteresis. *J. Phys. Chem. Lett.* **2014**, *5*, 2357–2363.

[46] Bube, R. H. Trap density determination by space-charge-limited currents. *J. Appl. Phys.* **1962**, *33*, 1733–1737.

[47] Poglitsch, A.; Weber, D. Dynamic disorder in methylammoniumtrihalogenoplumbates (II) observed by millimeter-wave spectroscopy. *J. Chem. Phys.* **1987**, *87*, 6373–6378.

[48] Xiao, Z. G.; Dong, Q. F.; Bi, C.; Shao, Y. C.; Yuan, Y. B.; Huang, J. S. Solvent annealing of perovskite-induced crystal growth for photovoltaic-device efficiency enhancement. *Adv. Mater.* **2014**, *26*, 6503–6509.

[49] Yang, D.; Yang, R. X.; Ren, X. D.; Zhu, X. J.; Yang, Z.; Li, C.; Liu, S. Z. Hysteresis-suppressed high-efficiency flexible perovskite solar cells using solid-state ionic-liquids for effective electron transport. *Adv. Mater.* **2016**, *28*, 5206–5213.